

Autophagy




ISSN: (Print) (Online) Journal homepage: www.tandfonline.com/journals/kaup20


The Wolfram-like variant WFS1^{E864K} destabilizes MAM and compromises autophagy and mitophagy in human and mice

Simone Patergnani, Méghane S. Bataillard, Alberto Danese, Stacy Alves, Chantal Cazevielle, René Valéro, Lisbeth Tranebjærg, Tangui Maurice, Paolo Pinton, Benjamin Delprat & Elodie M. Richard

To cite this article: Simone Patergnani, Méghane S. Bataillard, Alberto Danese, Stacy Alves, Chantal Cazevielle, René Valéro, Lisbeth Tranebjærg, Tangui Maurice, Paolo Pinton, Benjamin Delprat & Elodie M. Richard (23 Apr 2024): The Wolfram-like variant WFS1^{E864K} destabilizes MAM and compromises autophagy and mitophagy in human and mice, *Autophagy*, DOI: [10.1080/15548627.2024.2341588](https://doi.org/10.1080/15548627.2024.2341588)

To link to this article: <https://doi.org/10.1080/15548627.2024.2341588>

 View supplementary material 

 Published online: 23 Apr 2024.







 Submit your article to this journal 

 View related articles 

 View Crossmark data 



The Wolfram-like variant $WFS1^{E864K}$ destabilizes MAM and compromises autophagy and mitophagy in human and mice

Simone Patergnani ^{a*}, Méghane S. Bataillard^{b*}, Alberto Danese ^a, Stacy Alves^b, Chantal Cazevieille^c, René Valéro ^d, Lisbeth Tranebjærg^e, Tanguy Maurice^b, Paolo Pinton ^a, Benjamin Delprat ^{b*}, and Elodie M. Richard ^{b*}

^aDepartment of Medical Sciences, Section of Experimental Medicine, Technopole of Ferrara, Laboratory for Advanced Therapies (LTTA), Ferrara, Italy; ^bMMDN, University Montpellier, EPHE, INSERM, Montpellier, France; ^cINM, University Montpellier, INSERM, Montpellier, France; ^dDepartment of Nutrition, Metabolic Diseases and Endocrinology, Aix Marseille Univ, APHM, INSERM, INRAE, C2VN, University Hospital La Conception, Marseille, France; ^eThe Kennedy Center, Department of Clinical Genetics, Copenhagen University Hospital, Copenhagen, Denmark

ABSTRACT

Dominant variants in *WFS1* (wolframin ER transmembrane glycoprotein), the gene coding for a mitochondria-associated endoplasmic reticulum (ER) membrane (MAM) resident protein, have been associated with Wolfram-like syndrome (WLS). *In vitro* and *in vivo*, *WFS1* loss results in reduced ER to mitochondria calcium (Ca^{2+}) transfer, mitochondrial dysfunction, and enhanced macroautophagy/autophagy and mitophagy. However, in the WLS pathological context, whether the mutant protein triggers the same cellular processes is unknown. Here, we show that in human fibroblasts and murine neuronal cultures the WLS protein $WFS1^{E864K}$ leads to decreases in mitochondria bioenergetics and Ca^{2+} uptake, deregulation of the mitochondrial quality system mechanisms, and alteration of the autophagic flux. Moreover, in the *Wfs1^{E864K}* mouse, these alterations are concomitant with a decrease of MAM number. These findings reveal pathophysiological similarities between WS and WLS, highlighting the importance of *WFS1* for MAM's integrity and functionality. It may open new treatment perspectives for patients with WLS.

Abbreviations: BafA1: bafilomycin A₁; ER: endoplasmic reticulum; HSPA9/GRP75: heat shock protein family A (Hsp70) member 9; ITPR/IP₃R: inositol 1,4,5-trisphosphate receptor; MAM: mitochondria-associated endoplasmic reticulum membrane; MCU: mitochondrial calcium uniporter; MFN2: mitofusin 2; OCR: oxygen consumption rate; ROS: reactive oxygen species; ROT/AA: rotenone+antimycin A; VDAC1: voltage dependent anion channel 1; WLS: Wolfram-like syndrome; WS: Wolfram syndrome; WT: wild-type

ARTICLE HISTORY

Received 4 October 2023
Revised 3 April 2024
Accepted 8 April 2024

KEYWORDS

Autophagy; mitochondria-associated endoplasmic reticulum membrane; mitophagy; *WFS1*; Wolfram-like syndrome





Introduction

WFS1/Wolframin is a transmembrane protein, resident of the endoplasmic reticulum (ER) involved in cellular Ca^{2+} homeostasis and ER stress regulation [1]. Variants in *WFS1* have been associated with Wolfram syndrome (OMIM #222300), a severe and rare neurodegenerative disease characterized by juvenile-onset diabetes, optic atrophy and deafness, as well as a wide diversity of endocrine and neurological alterations [2,3].


Contrary to the recessive inheritance of WS, Wolfram-like syndrome (WLS, OMIM #614296) results from dominant *WFS1* variants and presents with the triad of symptoms that is progressive hearing loss, diabetes mellitus, and optic atrophy. Patients with WLS develop an overall milder phenotype, as there is few to no systemic manifestation leading to a shortened lifespan. However, vision and hearing capacities are severely impaired, with an earlier onset of the sensory deficits compared to WS patients. Even though no clear phenotype-genotype correlations can be made, the differences in symptomology between WS and WLS might

rely on the type of variant and their inheritance [4,5]. One can speculate that the dominant negative effect of missense variant associated with WLS might have increased toxicity in the sensory organs compared to the haploinsufficiency of biallelic nonsense variant associated with WS. Consistent with this hypothesis, in a mouse model, homozygous for the WLS *Wfs1^{E864K}* allele [6,7], we recently showed the devastating effect of this missense variant on the inner ear [8]. The homozygous mutant mice developed a profound post-natal hearing loss, at all tested frequencies, a collapse of the endocochlear potential and an alteration of the stria vascularis and neurosensory epithelium within their first month of age. While these effects might stem from an unbalanced ionic transfer due to a nonfunctional binding of *WFS1* to ATP1B1 (ATPase Na⁺/K⁺ transporting subunit beta 1), we cannot exclude that other mechanisms are taking place in a tissue-specific manner, as suggested by a recent literature review [5].

Indeed, *WFS1* variant associated pathologies were first considered as resulting from an alteration of the ER stress

CONTACT Elodie M. Richard  elodie.richard@umontpellier.fr  University Montpellier, EPHE, INSERM, Montpellier, France; Benjamin Delprat  benjamin.delprat@inserm.fr  University Montpellier, EPHE, INSERM, Montpellier, France

*These authors contributed equally.

 Supplemental data for this article can be accessed online at <https://doi.org/10.1080/15548627.2024.2341588>

response. As converging evidence, from independent studies, put light on the crucial role of WFS1 in Ca^{2+} dynamics at mitochondria-associated ER membranes (MAMs), leading eventually to mitochondrial bioenergetic deficits [9–11], they have recently been reclassified as “MAMopathies” [12]. Numerous studies, using a variety of WFS1 knockdown or deficient models ranging from eukaryotic cells – HEK cells [13], rat primary cortical neurons [9], *wfs1* null mouse-derived neuronal cultures [11], human patients’ fibroblasts [10], patients’ hiPSC-derived neurons [14] — to whole organisms — *wfs1* zebrafish [15,16] — indicate that WFS1 is a key player for proper mitochondrial functionality, in link with a dysregulation of Ca^{2+} homeostasis via altered transfer between ER and mitochondria at the MAMs. In addition, in rat primary neuronal cultures [9], *Wfs1* downregulation impaired mitochondrial dynamics and led to mitophagy, a selective process that removed aged and damaged mitochondria. Similarly, in fibroblasts derived from WS patients, we have previously shown that loss of WFS1 increased not only the mitophagic processes but also the autophagic ones, both critical for proper mitochondrial functioning [11].

In contrast with WS pathophysiology, which has attracted attention in the recent years, little is known about the underlying molecular mechanisms of WLS and the impact of the WLS specific *WFS1* variants. In the present study, we put in light the molecular role of WFS1 in a pathophysiological context of WLS in the central nervous system of a mouse model of the disease [8], *Wfs1*^{E864K}, and in patients’ fibroblasts [7], all harboring the missense variant WFS1^{E864K}.

Results

In mouse and *in vitro* human models of WS, WFS1 deficiency has been associated with Ca^{2+} homeostasis alteration, mitochondrial dynamics impairment and decreased ER-mitochondria contacts, leading to increased autophagy and mitophagy [10,11]. Patients with WLS present with less severe central deficits and one can question the impact of the disease-causing variant on the molecular pathways underlying the pathology.

To determine the functional impact of *Wfs1*^{E864K}, a WLS-associated protein [6,7], we first investigated the mitochondrial respiration, using a Seahorse XFe analyzer, of neuronal cultures from the hippocampus and cortex of wild-type (WT) and homozygous mutant mice, *Wfs1*^{E864K}, at post-natal day 33, age for which the neurosensorial deficits are at their maximal severity [8] (Figure 1A). We recorded a significant decrease of the basal ($p = 0.005$ and $p < 0.0001$; Figure 1B), ATP-related ($p = 0.0018$ and $p = 0.0002$; Figure 1C) and maximal ($p = 0.0025$ and $p = 0.0004$; Figure 1D) oxygen consumption rates of the neuronal cultures from the mutant mice, derived from both structures, compared to those of the cultures derived from WT mice. Likewise, we assessed directly on patients’ fibroblasts, heterozygous for the *WFS1*^{E864K} variant, the impact of the WFS1^{E864K} mutant protein on the mitochondrial respiration (Figure 1E). Comparing control and patients’ fibroblasts, we measured a significant decrease of the basal ($p = 0.019$; Figure 1F), ATP-related ($p = 0.0448$; Figure 1G) and

maximal ($p = 0.0496$; Figure 1H) oxygen consumption rates, as observed in mouse derived neuronal cultures.

In previous studies of WS models [9–11], the alteration of the mitochondrial functionality was associated with an impaired Ca^{2+} transfer between the ER and the mitochondria. Therefore, to assess the Ca^{2+} dynamics, we performed aequorin experiments in neuronal cells stimulated with 10 μM glutamate. In response to glutamate, Ca^{2+} uptake from the mitochondria was significantly decreased ($p < 0.0001$ and $p = 0.0022$; Figure 1I). However, unlike the experiments on WS model [10,11], Ca^{2+} release from the ER into the cytosol was not affected in mutant neuronal cells compared to the WT cells (Figure 1J), pointing toward a mitochondrial defect rather than an ER alteration. Moreover, in mutant and WT mice, we used transmission electron microscopy that allows a direct visualization of the MAMs, the contact zone between the ER and the mitochondria, to evaluate a potential structural alteration (Figure 1K). In the cortex of *Wfs1*^{E864K} mice, the density of mitochondria per neuron was similar to that of the controls (Figure 1L). However, the number of contacts between the mitochondria and the ER was significantly reduced in the mutants (62% decrease in mutant cells compared to WT, $p = 0.0042$; Figure 1M), recapitulating what we observed in WS models [11].

To confirm this alteration, we assessed the contact between the 2 organelles by immunofluorescence assays, using specific organelles’ markers (SEC61B/Sec61 beta pAcGFP-C1 plasmid for the ER [17], MitoTracker for the mitochondria) (Figure 1N,O). Analysis of the colocalization of the 2 organelles showed a decrease in the overlap coefficient in mutant cortical neuronal cells compared to WT cells ($p = 0.0042$; Figure 1O), corroborating the results we obtained with transmission electron microscopy.

Using TEM images, we, then, investigated the morphology of both the mitochondria and the ER, as any alteration of their shape might explain the reduction of contact sites. The total area of the mitochondria is not statistically different between WT and mutant conditions (Figure 1P). However, a slight decrease of the perimeter and maximal length was measured, along with an increase of the circularity index in the mutant mitochondria compared to WT ones (Figure S1). Overall, the mitochondria are “rounder” than their WT counterparts ($p = 0.0032$, Figure 1Q), reducing the interaction surface with the ER. To the contrary, an increase of the perimeter and maximal length of the ER was associated with a decrease of the circularity index in the mutant ER compared to WT (Figure S1). These measures imply an elongated ER, compensating for the altered shape of the mitochondria and facilitating their interaction. In addition, in mutant neuronal cells, the membranes and ridges of the mitochondria are less visible (Figure S1), suggesting an altered mitochondrial population. These morphological alterations, associated with structural defect of the MAMs and the decrease of the Ca^{2+} uptake by the mitochondria, are thus more likely responsible for the dysfunction of the mitochondrial respiration.

Dysfunctional and damaged mitochondria are removed by mitophagy, a specialized cellular process that selectively remove these organelles by autophagy [18]. We investigated mitophagy, first in the cultured neuronal cells using two fluorescent probes

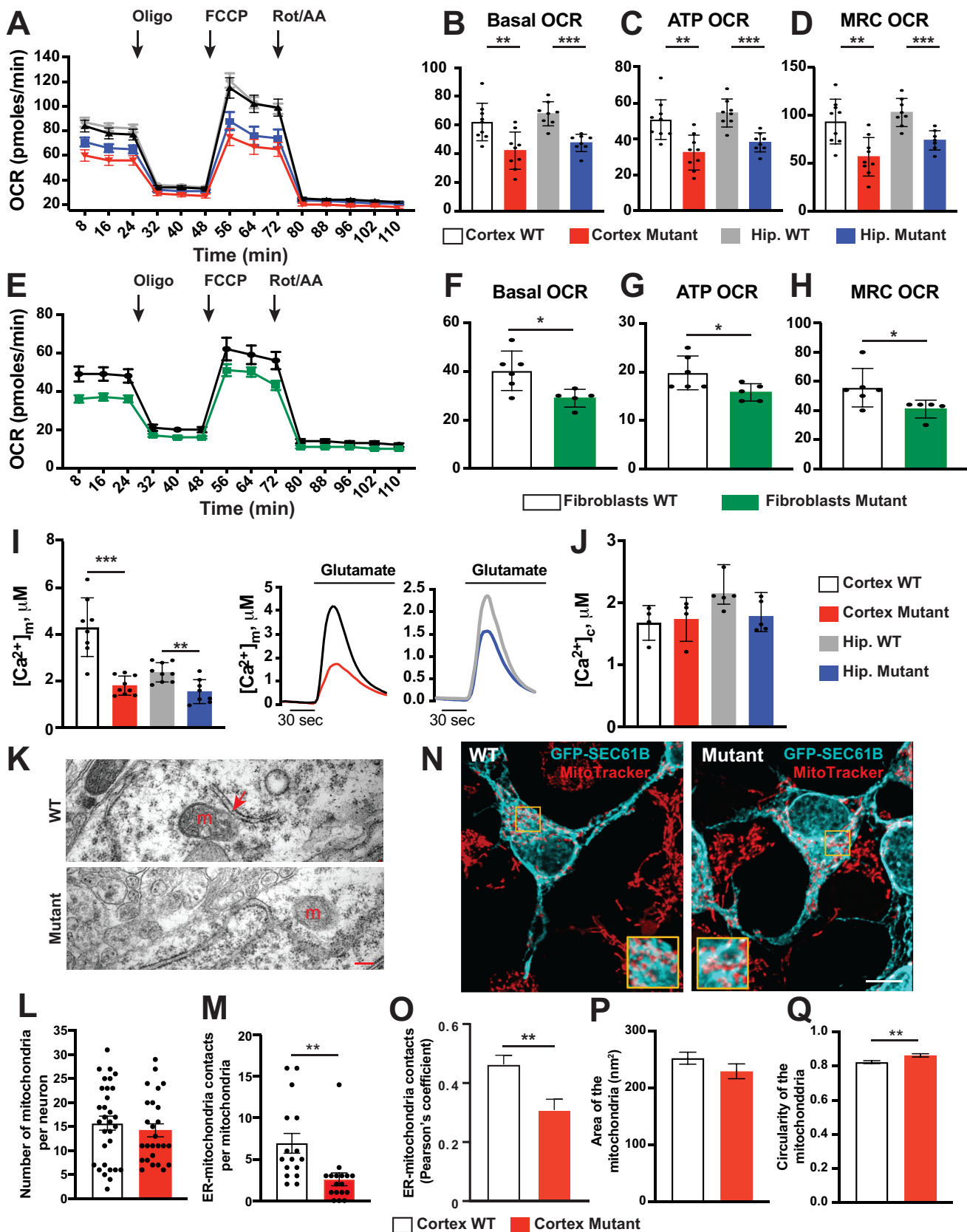


Figure 1. *Wfs1*^{E864K} protein leads to decreased mitochondrial respiration in patients' fibroblasts and *Wfs1*^{E864K} mutant mice, as well as altered Ca²⁺ transfer and a decrease of ER-mitochondria contacts in mice. (A-D) Oxygen consumption rate (OCR) traces of wild-type and mutant cortex and hippocampus (Hip.) neuronal cultures, expressed as picomoles of O₂ per minute, under basal conditions and after the injection of oligomycin (1.5 μM), FCCP (1 μM) and ROT/AA (1 μM). Quantification of basal (B), ATP-related (C) and maximal (D) respiration rates, calculated from OCR traces and expressed as means ± SD. (E-H) Oxygen consumption rate (OCR) traces of control (WT) and patient fibroblasts (Mutant), expressed as picomoles of O₂ per minute, under basal conditions and after the injection of oligomycin (1.5 μM), FCCP (1 μM) and ROT/AA (1 μM). Quantifications of basal (F), ATP-related (G) and maximal (H) respiration rates, calculated from OCR traces and expressed as means ± SD. (I-J) Representative traces of aequorin-based measurements of neurons obtained from cortex and hippocampi of *Wfs1* (WT, cortex: black line, hippocampus: gray line) and *Wfs1*^{E864K} (Mutant, cortex: red line, hippocampus: blue line) mice. Mitochondrial Ca²⁺ (I) and cytosolic Ca²⁺ (J) uptake measured

to label the lysosomes (LysoTracker) and mitochondria (MitoTracker) (Figure 2A). Confocal microscopy analysis revealed that in mutant neuronal cultured cells, the number of colocalizing dots was significantly increased compared to the number in the WT cells ($p < 0.0001$; Figure 2B). Mitophagy is tightly linked to mitochondria biogenesis and turnover which allow the replacement of altered mitochondria and ultimately the maintenance of the pool of healthy mitochondria. Cells were transfected with MitoTimer [19], a fluorescent protein used to assess mitochondria turnover by labeling in green newly synthesized mitochondria while the fluorescence shifts to red in aged mitochondria (Figure 2C). Measures of the green and red fluorescent intensities in all cultured neuronal cells indicate that mitochondria in the mutant cells, from both hippocampal and cortical neurons, are older than in the WT cells ($p < 0.0001$, $p < 0.0001$; Figure 2D).

In patients' fibroblasts, even though less marked than in murine neuronal cells, we found an increase of the MitoTracker-LysoTracker colocalizing dots ($p = 0.0252$) in the mutant compared to the control human cells (Figure 2E, F). Similar to the study in mouse derived neuronal cells, MitoTimer experiments performed in patients' fibroblasts lead to the conclusion of an older mitochondrial population in cells carrying the *WFS1*^{E864K} variant compared to controls ($p < 0.0001$; Figure 2G,H).

The increase of reactive oxygen species (ROS) in mitochondria is known to contribute to mitochondrial damages. When measured in *WFS1*^{E864K} physiopathological context, levels of mitochondrial ROS are increased in cultured cortical neurons ($p < 0.0001$; Figure 2I) as well as in patients' fibroblasts ($p < 0.0001$; Figure 2J), compared to the control cells. Taken together, our data demonstrate that in mutant cells, from both mouse and human, there is an accumulation of a deteriorated mitochondrial population, most likely due to an impairment of the elimination process.

In WS, the absence of *WFS1* is associated with an enhanced autophagy [11] linked to an unbalanced Ca^{2+} homeostasis. This dysregulation could be observed in primary cultures of hippocampal and cortical neurons from *Wfs1*^{E864K} mice. Cultured neurons were collected for immunoblot using the specific autophagic markers MAP1LC3/LC3 (microtubule-associated protein 1 light chain 3) and SQSTM1/p62, respectively used for the detection of the early and late steps of the autophagy process (Figure 3A). Interestingly, we found an increase of SQSTM1 level (Figure 3B), accompanied by a concomitant increased level of LC3-II (Figure 3C), the cleaved and lipidated form of LC3

related to the activation of the autophagic process, in the mutant cultured neurons ($p < 0.0001$, $p < 0.0001$ for SQSTM1 in hippocampal and cortical neurons; $p = 0.0004$, $p < 0.0001$ for LC3-II in hippocampal and cortical neurons). Similar increases were observed in fibroblasts from WLS patients by western blot analysis ($p = 0.0039$ for SQSTM1, $p = 0.0074$ for LC3-II; Figure 3D-F). The elevated amount of LC3-II measured by western blot was then confirmed by transfecting mutant cells (Figure S2A-B) the specific fluorescent marker of the autophagosomes: the GFP-LC3 (GFP-LC3^{vac} [20]) construct ($p < 0.0001$).

A simultaneous increase of both the cleaved form of LC3 and SQSTM1 has been frequently associated with a dysregulation of the autophagic flux, in which the autophagosomes are continuously created (LC3-II increase) but they struggle to be degraded (SQSTM1 accumulation) [21]. To discriminate whether the impact of the mutant *WFS1*^{E864K} protein on the autophagic processes is due to an activation of the autophagic flux or an inhibition of the autophagosome-lysosome fusion, we performed experiments using the tandem fluorescent construct mCherry-GFP-LC3 (capable of tracking the different stages of autophagy) and by treating cells with bafilomycin A₁ (BafA1), an antibiotic which impairs the autophagosome-lysosome fusion and autolysosome acidification, the late steps in the autophagic process, blocking the autophagic flux [21]. Fluorescence microscopy analysis of the punctate structures after BafA1 treatment suggests that mutant *WFS1* protein, rather than activating a sustained autophagosome formation process, alters and slows down the autophagy flux. Indeed, post BafA1 treatment, the autophagosome population increased in both conditions, WT and mutant cells, however the increase in the mutant is comparatively lower than in the WT: +17% and +28% in the mutant cells vs. +310% and +240% in the WT cells, for cultured neurons and fibroblasts respectively (Figure 3G-J). Likewise, the autolysosome population decreased in both conditions; however, the decrease in the mutant is comparatively lower than in the WT: -27% and -24% in the mutant cells vs. -80% and -57% in the WT cells, for cultured neurons and fibroblasts respectively (Figure 3G-J). Immunoblot analyzes of LC3-II and SQSTM1 levels in treated and non-treated cells highlight an increase of these proteins in all treated cells (Figure 3K-N, Figure S2E-F). However, akin to what we observed in immunofluorescence microscopy analyzes, while the amounts of SQSTM1 and LC3-II, in the WT cells, are increased by 2- and 3-fold respectively, the increase of these autophagic markers in mutant cells is less than 1.25-fold. Moreover, there is

after 10 μ M glutamate stimulation. Quantification of mitochondrial Ca^{2+} (I) and cytosolic Ca^{2+} uptake (J), expressed as means \pm SD, for hippocampus and cortex neuronal cultures of *Wfs1* and *Wfs1*^{E864K} (mutant) mice. (K-M) Transmission electron micrographs of cortical neurons from three mutant and three WT mice. Contact between ER and outer membrane of a mitochondrion with a distance smaller than 30 nm is pointed by the red arrow. m: mitochondria, scale bar: 200 nm. Quantification of the number of mitochondria per neuron (L) and number of mitochondria in contact with ER (distance <30 nm) (M), data are expressed as means \pm SEM. (N-O) Colocalization of mitochondria and lysosomes in cultured cortical neurons from mutant and WT mice. (N) Representative images of a 3D reconstructed picture of *Wfs1* and *Wfs1*^{E864K} (mutant) cortex neurons transfected with the ER marker SEC61B/Sec61 beta pAcGFP-C1 (GFP-SEC61B, cyan) and loaded with the mitochondrial marker MitoTracker (red), scale bar: 10 μ m. The insets are a 2-fold magnification of the boxed areas. (O) Calculation of the colocalization rate between ER and mitochondria, using Pearson's coefficient, data are expressed as means \pm SEM. The total area (P) and the circularity of the mitochondria (Q) were also measured on the transmission electron micrographs of cortical neurons. Data are expressed as means \pm SEM. All tested animals were at 33-days-old at the time of experimentation. Per group, $n = 8-9$ for (B-D), $n = 5-6$ for (F-H), $n = 4$ for (I), $n = 8-9$ for (J) $n = 24$ (8 technical replicates and 3 biological replicates) for (L), $n = 16$ (8 technical replicates and 2 biological replicates) for (M), $n = 17$ for (O), and $n = 353$ mitochondria for WT and $n = 187$ for mutant for (P) and (Q). Unpaired t-tests: * $p < 0.05$, ** $p < 0.01$, *** $p < 0.001$. Oligo, oligomycin; FCCP, carbonyl cyanide-4(trifluoromethoxy)phenylhydrazine; Rot/AA, rotenone+antimycin A.

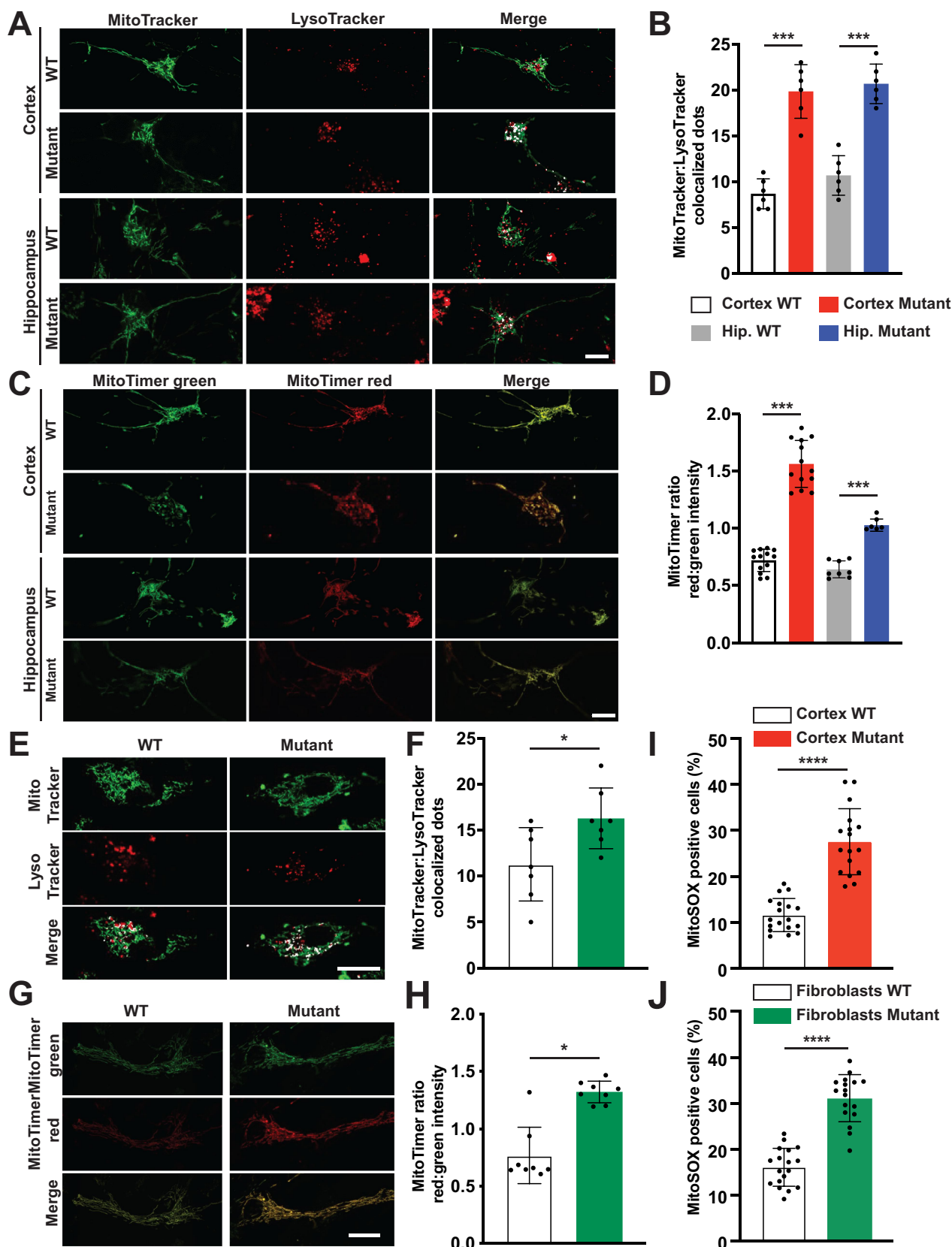


Figure 2. WFS1^{E864K} protein alters mitophagy and is associated with an older mitochondrial population in fibroblasts from patient with WLS and neuronal cultures derived from WLS mouse model cortex and hippocampi. (A-B) Mitophagy activation assessment: (A) Confocal microscopy images of wild-type (WT) and mutant cortex and hippocampus (Hip.) neuronal cultures labeled with mitochondrial (MitoTracker, green) and lysosomal (LysoTracker, red) markers and quantification of the colocalization dots (B). (C-D) MitoTimer measurements of mitochondrial age WT and mutant cortex and hippocampus neuronal cultures: (C) Representative confocal fluorescent images of the green, the red channels, and the merge. (D) Quantification of the red:green intensities ratio. (E-F) Mitophagy activation assessment: (E) Confocal microscopy images of fibroblasts labeled with mitochondrial (MitoTracker, green) and lysosomal (LysoTracker, red) markers and quantification of the colocalization dots (F). (G-H) Mitochondria turnover assessment using MitoTimer measurements in fibroblasts: (G) Representative epifluorescent images of the green, the red channels, and the merge. (H) Quantification of the red:green intensities ratio. (I-J) Quantification of MitoSOX-positive cells in WT and mutant cortex neuronal cultures (I) and fibroblasts (J). Data are expressed as means \pm SD. Each value is the mean of $n = 6$ per condition in (B), $n = 8-13$ in (D), $n = 7$ in (F), $n = 8$ in (H), $n = 18$ in (I) and (J). Scale bar: 10 μ m for all panels in (A) and (C), 20 μ m for all panels in (E) and (G). Unpaired t-tests: * $p < 0.05$, *** $p < 0.001$, **** $p < 0.0001$.

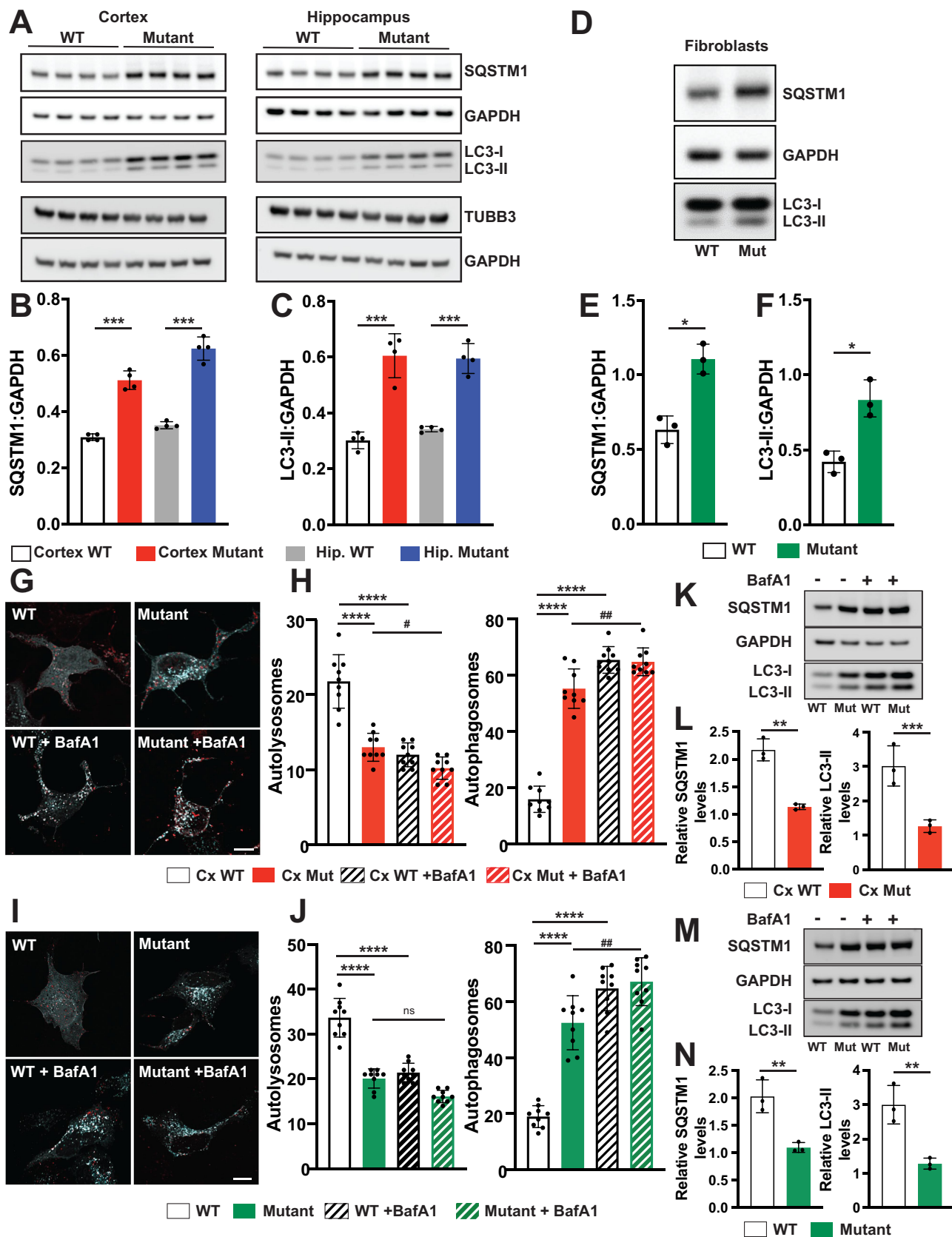


Figure 3. *WFS1*^{E864K} protein induces an altered autophagy flux in mouse neurons and fibroblasts. (A–C) Autophagy in neuronal cultures derived from *Wfs1*^{E864K} mice: (A) Representative immunoblot showing the increase of SQSTM1 and the autophagic form of LC3 (LC3-II) in neurons cultured from the cortex and hippocampus (Hip.) of *Wfs1* (WT) and *Wfs1*^{E864K} (mutant) mice. The purity of neuronal cultures was assessed with immunoblot against the neuronal marker TUBB3/ β 3-tubulin. GAPDH was used as loading control. Densitometry ratios of SQSTM1 and LC3-II over GAPDH are shown in (B) and (C). Data are expressed as means \pm SD. (D–F) Autophagy in patient’s fibroblasts: (D) Representative immunoblot showing the increase of SQSTM1 and LC3 lipidation in fibroblasts from control (WT) and patient harboring the *WFS1*^{E864K} variant (Mut). GAPDH was used as loading control. Densitometry ratios of SQSTM1 and LC3-II over GAPDH are shown in (E) and (F). Data are expressed as means \pm SD. (G–H) Autophagy flux in neuronal cultures derived from *Wfs1*^{E864K} mice: (G) Representative images of 3D reconstructed fluorescence microscopy

not statistically significant differences between SQSTM1 and LC3-II amounts in BafA1-treated WT cells compared with BafA1-treated mutant cells (Figure S2C-F). Overall, these data clearly indicated that rather than an activation of the autophagy process *per se*, the mutant protein might interfere with the autophagy flux, compromising the maturation of the autophagosomes.

Discussion

WFS1-associated disorders encompass a spectrum of rare pathologies [22], recently termed “wolframinopathies” by de Muijnck and colleagues [5]. Wolfram syndrome is the most common one even though its worldwide prevalence is estimated to approximately 1 in 770,000 [2]. WFS1 biallelic recessive variants are responsible for WS type 1. Given the resemblance of WS symptoms with mitochondrial diseases, mitochondrial functionality was studied in different models of the syndrome and highlighted the key role of WFS1 in mitochondrial bioenergetics [9,11,13–16]. However, WFS1 expression was either abolished or knocked down in these models, leading to a low level up to the complete absence of WFS1 protein. In the context of WLS, the mutant protein is expressed, along the WT protein, so the molecular mechanism(s) underlying the pathology might be different.

In our study, we determined that WLS protein WFS1^{E864K} is associated with mitochondrial bioenergetic deficits, both in murine neuronal cells and fibroblasts derived from WLS patients. These results were comparable to the one obtained in similar cellular models of WFS1 loss [10,11]. One explanation for altered energy production is a dysregulated Ca²⁺ homeostasis, as observed in various WS models. Contrary to what we previously reported in WS cellular models, cytosolic Ca²⁺ was not different between WT and mutant cells suggesting a normal ER efflux of Ca²⁺. However, mitochondrial Ca²⁺ uptake was decreased in mutant neuronal cell lines, pointing toward an alteration at the mitochondria level rather than from the ER. This reduced uptake, associated with normal intracellular Ca²⁺ dynamics, can be explained by a decreased interaction between these 2 organelles. Indeed, despite a similar number of mitochondria per neuron, the number of contacts between the mitochondria and the ER, defining the number of MAMs, is lower in mutant cortical neurons compared to WT

cells. At the ER-mitochondria cleft, Ca²⁺ stored in the ER is released by the ITPRs (inositol 1,4,5-trisphosphate receptors), then transported to VDAC1 (voltage dependent anion channel 1) by HSPA9/GRP75 (heat shock protein family A (Hsp70) member 9), with MCU (mitochondrial calcium uniporter) eventually channeling the cations to the mitochondrial matrix [23]. We specifically looked at contacts with a distance of less than or equal to 30 nm, the width necessary to allow correct assembly of the ITPR-HSPA9-VDAC1 complex, responsible for Ca²⁺ flux [24]. Consequently, we can speculate that this diminished interaction can adversely affect Ca²⁺ transfer and homeostasis, even though we cannot exclude a change in mitochondria membrane potential or in expression level of mitochondria Ca²⁺ uptake machinery [25].

Samples obtained from mutated mice and fibroblasts from WLS patients displayed an accumulation of deteriorated mitochondrial population, as demonstrated by the presence of important mitochondrial deficits, including reduced Ca²⁺ uptake, respiration, and increases of the amount of mitochondrial ROS. In addition, we noted that in the mutated condition the mitochondrial turnover rates were reduced, thereby demonstrating the existence of an aged mitochondria population, which can be caused by an impaired capacity of the cells to remove efficiently damaged mitochondria.

This impairment might stem from an alteration of the autophagy flux as shown by the increase of autophagosome processes in mutant cells, which could be determined to a deficient ER-mitochondria coupling in these cells. The origin of the autophagosome membrane is still under debate, however, ample evidence suggest that autophagy begins at the MAMs [26]. They would play a dual role as a platform for autophagy related proteins to perform their biological function and as a modulator of the Ca²⁺ homeostasis and lipid metabolism which are both key for autophagosome development [26,27]. Indeed, unbalanced Ca²⁺ homeostasis between ER and mitochondria has been shown to activate pro-survival autophagy at MAM level [28,29]. A decrease of Ca²⁺ transfer from the ER to the mitochondria was shown to activate AMPK translocation to MAMs which would activate autophagy processes via the BECN1 protein [30].

A conserved MAM integrity is also crucial for the regulation of mitophagy [31]. Consistently, MAMs disruption or loss of function of the activity of proteins localized at these contact points may lead to defective autophagy processes and

acquisition of cortical neurons transfected with the LC3-tandem mCherry-GFP-LC3 plasmid. Autolysosomes are labeled in red (mCherry⁺; GFP⁻) and autophagosomes in white (mCherry⁺; GFP⁺). To note, to enhance the visualization of the dots, GFP-positive cells are labeled in cyan. To mimic a blockage of the autophagic flux, 100 nM bafilomycin A₁ (BafA1) was added for 2 h. (H) Quantification of autolysosomes (mCherry⁺; GFP⁻ cells) and autophagosomes (mCherry⁺; GFP⁺) per cortical neuron-derived cell, expressed as means ± SD. (I-J) Autophagy flux in patient's fibroblasts: (I) Representative images of 3D reconstructed fluorescence microscopy acquisition of fibroblasts transfected with the LC3-tandem mCherry-GFP-LC3 plasmid. Autolysosomes are labeled in red (mCherry⁺; GFP⁻) and autophagosomes in white (mCherry⁺; GFP⁺). To note, to enhance the visualization of the dots, GFP positive cells are labeled in cyan. To mimic a blockage of the autophagic flux, 100 nM bafilomycin A₁ (BafA1) was added for 2 h. (J) Quantification of autolysosomes (mCherry⁺; GFP⁻ cells) and autophagosomes (mCherry⁺; GFP⁺) per fibroblast, expressed as means ± SD. (K) Representative immunoblots showing the increase of SQSTM1 and LC3-II after the inhibition of the autophagic flux using BafA1 in neuronal cultures derived from *Wfs1*^{E864K} mice and their quantification (L). The intensities of SQSTM1 and LC3-II bands after BafA1 treatment (BafA1⁺) are expressed in fold increase of the intensity of these bands in resting conditions (BafA1⁻). The intensity of each band was first normalized against the intensity of the GAPDH band (loading control). Data are expressed as means ± SD. (M) Representative immunoblots showing the increase of SQSTM1 and LC3-II after the inhibition of the autophagic flux using BafA1 in patient's fibroblasts and their quantification. (N) The intensities of SQSTM1 and LC3-II bands after BafA1 treatment (BafA1⁺) are expressed in fold increase of the intensity of these bands in resting conditions (BafA1⁻). The intensity of each band was first normalized against the intensity of the GAPDH band (loading control). Data are expressed as means ± SD. Each value is the mean of *n* = 4 per condition in (B, C), *n* = 3 in (E, F), *n* = 9 in (H, L) and *n* = 3 in (J, N). Scale bar: 10 μm. Unpaired t-tests for (B-C), (E-F), (L) and (M): **p* < 0.05, ***p* < 0.01, ****p* < 0.001. Two-way ANOVA followed by Tukey's multiple comparisons test for (H) and (J): *p* < 0.0001 for the genotype, *p* < 0.0001 for the BafA1 treatment, *****p* < 0.001 vs. WT, #*p* < 0.05, ##*p* < 0.01, ns = non-significant vs. mutant.

a pathological condition [31,32]. Thus, the altered MAM integrity and function in *WFS1*^{E864K} fibroblasts and neuronal cells might be leading to an increase of autophagy markers and consequently the alteration of mitochondrial functions. We showed in WS patients' fibroblasts that the absence of WFS1 activated both mitophagy and autophagy processes [11]. Nonetheless, contrary to what was observed in *WFS1* null fibroblasts, when the autophagy flux is blocked using BafA1, the relative rise of autophagosomes is less in the mutant than in the WT fibroblasts and cultured cortical neurons. These results might indicate that, in basal conditions, the autophagy flux is not totally inhibited but rather deeply affected. Consequently, the resulting accumulation of autophagosomes and the difficulty in eliminating impaired mitochondria could be the cause of the mutation-driven phenotype. Moreover, a compromised autophagy is detrimental for neuronal cells, often time associated with neurodegeneration [33], as reported not only in the pathophysiological context of WS [9,15] but also other neurodegenerative disorders [18]. The attenuated dysregulation of autophagy in WLS models, compared to the one observed in knock-out cells, might explain why no degeneration has been reported so far in WLS patients [5]. However, the rarity of the disease and the underdiagnose of the population might have hampered an extended characterization of the symptomology of WLS, more particularly in aged patients. Akin to what we reported in WS models [10,11], overall, the decreased number of MAMs is triggering an alteration of the cellular bioenergetics and a deregulation of ER-mitochondria crosstalk. These cellular and molecular abnormalities have been reported for neurodegenerative disorders such as Alzheimer, Parkinson and Huntington diseases, and amyotrophic lateral sclerosis, among others [27,34–36]. In addition, new studies highlighted the potential role of WFS1 itself in central nervous system neurodegeneration and more particularly Alzheimer disease [9,37]. Thus, even though the severe vestibular syndrome of *Wfs1*^{E864K} mice is preventing us to explore their potential behavioral deficits, in light of these shared common mechanisms underlying WS, WLS and the other neurodegenerative disorders, it would be of great interest to look at aged mice to investigate potential neurodegenerative processes.

While the importance of WFS1 for proper MAM function has been well established using *in vitro* and *in vivo* models, its role(s) in the structure of the MAM remain unknown. In mouse and human, WFS1 regulates the number of contacts between the ER and the mitochondria [10,11]. One explanation could be that WFS1 modulates tethering proteins, warrants of the structural integrity of the MAMs. Indeed, the combination of optic atrophy and hearing loss is the clinical hallmark of WLS, but also dominant optic atrophy and deafness/DOAD (OMIM #125250). Variants in *OPA1* (*OPA1* mitochondrial dynamin like GTPase) are mainly responsible for dominant optic atrophy and deafness [38]. This protein, anchored to the mitochondrial inner membrane facing the inter-membrane space, plays a critical role in mitochondria, as a link between the mitochondrial structure and bioenergetic functions, regulating mitochondrial fusion [39]. This fusion process of mitochondrial membranes is promoted by the binding of *OPA1* and the mitochondria-bound MFN2

(mitofusin 2), a key tethering protein of the MAMs (for review [40]). In the absence of WFS1, in rat and patients' fibroblasts, no change of *MFN2* expression level was reported [9,10]. However, due to the similarities between dominant optic atrophy and deafness and WSL symptoms, one can ask if the Ca²⁺ homeostasis and MAM alteration in WSL might be due to tethering abnormalities rather than stemming primarily from ITPR-HSPA9-VDAC1 complex function alteration. In addition, WFS1 is interacting with several MAM resident proteins such as SIGMAR1/S1R (sigma non-opioid intracellular receptor 1) [11], NCS1 (neuronal calcium sensor 1) [10] and VDAC1 itself [14], which all have a role in MAM structure as well as function. Even though we cannot qualify VDAC1 role as classical tethering, it works as a contact site spacing or filling function through its interaction with HSPA9 and ITPR [14]. SIGMAR1 and NCS1 stabilize MAMs by interacting with ITPR and/or VDAC1 [26,41]. Variants in WFS1 might impact the binding to its protein partners leading to aberrant MAM structure and function.

Overall, in murine neuronal cells and patients' fibroblasts, our findings indicate that *WFS1*^{E864K} protein leads to aberrant Ca²⁺ homeostasis, mitochondrial bioenergetics deficits, deregulation of autophagy associated with MAM alterations. Our findings suggest considering the use of the same therapeutic targets as for WS in a WLS context, combined with autophagy inducers to ameliorate the outcome, thus opening treatment perspectives that were previously non-existent.

Materials and methods

Fibroblasts culture

This study followed the tenets of the Declaration of Helsinki. Primary cultures of human dermal fibroblasts were established from skin biopsies taken after obtaining informed consent from one individual without diabetes mellitus and one affected patient carrying the c.2590 G>A (E864K) variant in *WFS1* gene, as previously described [42]. Fibroblasts from these skin explants were cultured in Dulbecco modified Eagle's medium (DMEM; Euroclone, ECB7501L) supplemented with glucose (4.5 g l⁻¹), 2 mM l-glutamine (Euroclone, ECB3000D), 10% (v: v) fetal bovine serum (FBS; Gibco, A5256701) and 1% penicillin-streptomycin. All the experiments were performed on fibroblasts between tissue culture passages 4 and 12.

Transfection with the autophagy reporters GFP-LC3 [20], mCherry-GFP-LC3 [20] and the indicator of mitochondrial turnover pTRE-tight-MITO TIMER [43] was performed using Lipofectamine LTX&PLUS (Thermo Fisher Scientific 15338–100).

Mouse breeding

The *Wfs1*^{E864K} mice were generated as previously described [8]. Animal care and experimentation were authorized by the National Ethic Committee (Paris) and carried out in strict adherence to the European Union Directive 2010/63 and ARRIVE guidelines [44]. Mice were housed in cages with free access to water and food. The rooms were temperature-

controlled, lit on a 12:12 h light/dark cycle, lights on at 7:00 h. All experiments were performed during the light cycle, at the same time.

Isolation of neurons from *Wfs1* and *Wfs1*^{E864K} hippocampi and cortex

Primary neuronal cultures were obtained from brains of adult mice as reported in [11]. Briefly, after isolation from the brains, hippocampi and cortex were first mechanically and then enzymatically dissociated at 37°C for 15 min in a solution of 0.25% (wt:vol) trypsin and 10 µg/ml DNase. After filtration with a 70-µm pore cell strainer (Fisher scientific, 08-771-2), the cellular homogenates obtained were cultured in neuronal culture medium Neurobasal (Thermo Fisher Scientific 21,103-049) enriched with B27 supplement (Thermo Fisher Scientific 17504-044), 1% penicillin-streptomycin and 0.5 mM Glutamax (Gibco, 35050-038). To avoid the proliferation of non-neuronal cells, cytosine arabinoside (1 µM; Merck, C1768) was added to the cultures after 24 h from the plating. Immunoblot assays against specific neuronal markers TUBB3/β3-tubulin (Cell Signaling Technology, 5568) permitted to assess the purity of cell cultures.

Determination of cellular oxygen consumption rate (OCR)

Cells were seeded in a 96-well microplate at a density of 2×10^4 cells/well and cultured in DMEM high glucose supplemented with 10% FBS, 1% penicillin-streptomycin and 1% glutamine. Culture medium was then changed with XF Assay Medium (Agilent, 102353-100) supplemented with glucose (Merck, G7528), sodium pyruvate (Merck, P5280) and glutamine (Euroclone, ECB3000D) (175 µL per well, pH = 7.4) and equilibrated at 37°C without CO₂. After 1 h, OCR was registered using a Seahorse XFe96 extracellular flux analyzer (Seahorse Bioscience), as follows: after performing the baseline measurement, oligomycin (1.5 µM; Agilent, 103015-100), carbonyl cyanide 4-(trifluoromethoxy)phenylhydrazine (FCCP, 1 µM; Agilent, 103015-100) and rotenone+antimycin A (ROT/AA, 1 µM; Agilent, 103015-100) were successively injected while measuring OCR. Basal respiration was calculated by removing the OCR values after ROT/AA injection to the OCR measured before oligomycin treatment. ATP production was defined as the difference between basal respiration and the OCR registered after oligomycin injection. The maximal respiration rate represents the value obtained by subtracting the value registered after ROT/AA injection to the OCR after FCCP treatment. All data were normalized to the total cell number obtained by staining cells with crystal violet method.

Aequorin measurements

Cells were seeded on 13-mm glass coverslips and transfected with adenoviral construct encoding a cytosolic and mitochondria-targeted aequorin. 36 hours post-infection, cells were reconstituted for 2 h with 5 µM coelenterazine WT (Calbiochem, CAS 55779-48-1) in DMEM high glucose

supplemented of 0.1% FBS and transferred to the perfusion chamber. Measurements were performed in Krebs-Ringer buffer (135 mM NaCl, 5 mM KCl, 1 mM MgSO₄, 0.4 mM KH₂PO₄, 20 mM HEPES, pH 7.4) supplemented with 5 mM glucose and 1 mM CaCl₂. Ca²⁺ release from the intracellular stores and the consequent cytosolic and mitochondrial Ca²⁺ accumulation was induced by adding the Ca²⁺-mobilizing agent glutamate (10 µM; Merck, G1626). After this stimulation, cells were lysed with 100 µM digitonin (Merck, 300410) in a hypotonic Ca²⁺-rich solution (10 mM CaCl₂ in H₂O), to discharge the remaining aequorin pool. Finally, the light signal detected was collected and calibrated into Ca²⁺ values by using a specific algorithm, as described in [45].

MAM analysis

Transmission electron microscopy

Morphological changes were investigated using TEM analyzes. *Wfs1* (WT) and *Wfs1*^{E864K} homozygous mice were perfused intracardially with a 4% paraformaldehyde solution at room temperature ($n = 3$ mice per genotype). Small fragments (about 1 mm³) of the cortex from the brain of each mouse were extracted and immersed in a solution of 2.5% glutaraldehyde in PHEM buffer (1X, pH 7.4; Electron Microscopy Sciences, 11162) overnight at 4°C. They were then rinsed in PHEM buffer and post-fixed in a 0.5% osmic acid + 0.8% potassium hexacyanoferrate trihydrate for 2 h at dark and room temperature. After two rinses in PHEM buffer, the cells were dehydrated in a graded series of ethanol solutions (30–100%). The tissues were embedded in EMbed 812 (Electron Microscopy Sciences, 14120) using an Automated Microwave Tissue Processor for Electronic Microscopy (Leica, Wetzlar, Germany). Thin sections (70 nm; Leica-Reichert Ultracut E) were collected at different levels of each block. These sections were counterstained with uranyl acetate 1.5% in 70% ethanol and lead citrate and observed using a Tecnai F20 transmission electron microscope (FEI company, Hillsboro, OR, USA).

To evaluate the frequency of contact between the mitochondria and the ER in the different neurons, we photographed at 5,800 × magnification, all the cytoplasmic area from 8 different neurons in each of 6 samples with a Tecnai F20 transmission electron microscope at 120 KV. From these images, we counted the number of mitochondria. We then randomly photographed at 25,500 × magnification, 8 different cytoplasmic areas, containing mitochondria, from the previous neurons. In each image, we counted the number of mitochondria and calculated the proportion of mitochondria in close contact with ER (<30 nm).

Mitochondrial measurements were performed by tracing the outer membrane of the mitochondria, as described in [46]. In brief, the area (mitochondrial surface), perimeter (length of the mitochondrial outline), circularity ($4\pi \text{ area}/\text{perimeter}^2$), maximal length (measurement of the main mitochondrial axis, Feret diameter) and minimal width (measurement of the minor mitochondrial axis, Feret diameter) of the profile were measured with ImageJ2 software (2.14.0/1.54f version). For each mitochondrion, we analyzed

organelle complexity by determining the visibility of inner/outer membranes and mitochondrial ridges. The scores assigned to these parameters are 1 if membranes/ridges are visible on more than 50% of the mitochondrion, 0 if membranes/ridges are not visible on more than 50% of the mitochondrion.

The same analyzes were performed on endoplasmic reticulum.

ER-Mitochondria contact sites analysis by immunofluorescence

After purification, cortex neurons were seeded on 24 mm glass coverslips and transfected with a plasmid encoding the ER marker SEC61B/Sec61 beta pAcGFP-C1 (Addgene, 62008; deposited by Eric Schirmer) and then loaded with the mitochondrial marker MitoTracker Red (200 nM; Thermo Fisher Scientific, M22425) for 15 min. Next, cells were acquired on an Olympus FV3000 confocal microscope equipped of a 63× oil immersion objective (N.A. 1.4) by taking z-series of 0.42 μm each to capture the entire volume of the cells.

Images obtained were then processed and analyzed by using ImageJ (Fiji) software, as follows: first, images were deconvolved by using the Richardson-Lucy Algorithm in the DeconvolutionLab2 plugin [47]. A Point Spread Function (PSF) specific for each wavelength was derived from the PSF generator plugin [48]. Second, after deconvolution, colocalization levels were quantified by Pearson's coefficient using the JACoP plugin [49]. To create representative items, deconvolved images were merged in cyan (ER) and red (mitochondria) and 3D reconstructed by using the 3D projection plugin.

Autophagy analyses

Western blot analyses

Primary antibodies used for the detection of the autophagic mechanisms by immunoblot were anti-LC3B antibody (Merck Group, L7543) and anti-SQSTM1/p62 (Merck Group, P0067). An anti-ACTB/beta-actin (Merck Group, A1978) antibody was used as loading marker.

Immunofluorescence analysis using GFP-LC3 construct

Autophagy was also detected by fluorescent microscopy by transfecting cells with a plasmid encoding a GFP-LC3 construct (kindly provided by Prof. Guido Kroemer, Institut Gustave-Roussy, Villejuif, France). Images were taken on an Olympus FV3000 confocal microscope (Olympus Corporation, Tokyo, Japan) equipped of a 63× oil immersion objective (N.A. 1.4). The number of GFP-LC3 dots was automatically counted by using ImageJ (Fiji) software. Where indicated, cells were treated for 2 h with 100 nM BafA1 (Merck, B1793), a potent inhibitor of the lysosomal V-ATPase, to mimic the inhibition of autophagosome-lysosome fusion, as reported in [50].

Autophagy flux analyses using mCherry-GFP-LC3 construct

Cells were seeded on 24 mm glass coverslips and transfected with the LC3-tandem plasmid mCherry-GFP-LC3 (kindly

provided by Prof. Paola Rusmini, Università degli Studi di Milano, Milan, Italy). Next, cells were acquired on an Olympus FV3000 confocal microscope equipped of a 63× oil immersion objective (N.A. 1.4) by taking z-series of 0.42 μm each to capture the entire volume of the cells.

Images obtained were then processed and analyzed by using ImageJ (Fiji) software, as follows. Images were deconvolved by using the Richardson-Lucy Algorithm in the DeconvolutionLab2 plugin [47]. A Point Spread Function (PSF) specific for each wavelength was derived from the PSF generator plugin [48]. After deconvolution, images of both channels were automatically thresholded with JACoP plugin to image the fluorescent signals arising only from the fluorescent dots [49]. Autolysosomes were quantified on the red channel as the exposure to the acidic environment of the lysosome diminished the GFP fluorescence, while the mCherry signal remained stable. Autophagosomes were quantified on the red⁺ and green⁺ channel. To create representative items, deconvolved images were merged in cyan (green channel) and red (red channel) and 3D reconstructed by using the 3D projection plugin. In these pictures, the colocalization signal appears in white.

Autophagy flux analyses using western blot

After 2-h treatment with 100 nM BafA1 to mimic the inhibition of autophagosome-lysosome fusion, cells were harvested and then lysed in modified 10 mM Tris buffer (pH 7.4) containing 150 mM NaCl, 1% Triton X-100 (Merck, T8787), 10% glycerol, 10 mM EDTA and protease (Merck, P8340) and phosphatase (Roche, 04-906-837-001) inhibitor cocktails. Protein extracts were quantified using the Lowry assay (Bio-Rad Laboratories, 500-0116). Fifteen μg of proteins of each condition were loaded on a precast 4–12% bis-Tris acrylamide gels and then transferred on a nitrocellulose membrane. After 1 h of blocking in nonfat milk 5%, membranes were incubated overnight at 4°C with specific antibodies. The next day, membranes were incubated with a goat-anti rabbit (Thermo Fisher Scientific, A16104) or a goat anti-mouse secondary antibody (Thermo Fisher Scientific, A16072) for 1 h at room temperature. After three washes, membranes were incubated with a chemiluminescent substrate and the signals acquired by using an ImageQUANT instrument (GE Healthcare). Densitometric analyzes were performed by using ImageJ (Fiji) software. The fold changes of the proteins of interest were normalized against the housekeeping protein GAPDH.

Mitophagy analyses

Cells were seeded on 24-mm glass coverslips and loaded with the mitochondrial and lysosomal fluorescent probes, MitoTracker Green FM (Thermo Fisher Scientific, M7514) and LysoTracker Red DND-99 (Thermo Fisher Scientific, L7528), respectively, for 15 min. Next, cells were taken by using a FV3000 Olympus confocal microscope with a 63× oil immersion objective (N.A. 1.4). Background was subtracted from the images and the colocalization rates were measured by using the colocalization plugin “Colocalization Thresholds” available with ImageJ (Fiji) software.

Mitochondrial ROS measurements

Briefly, cells were loaded with 5 μ M of MitoSOX (Thermo Fisher Scientific, L7528). After 30 min, fluorescence was measured at the TaliTM Image-Based Cytometer using 510 \pm 10 nm and 595 \pm 35 nm excitation and emission wavelengths, respectively. The levels of mitochondrial ROS in each condition were presented as the percentage of red positive cells on the total of cells counted for each field.

Analysis of mitochondrial turnover

Cells were seeded on 24 mm glass coverslips and then transfected with the pTRE-tight-MITO TIMER plasmid (Addgene, 50547; deposited by Roberta Gottlieb). Cells were imaged using excitation at 488 nm and emission of 513 for the green channel and at 561 nm and emission at 586 nm for red channel with a FV3000 Olympus confocal microscope with a 63 \times oil immersion objective (N.A. 1.4). Ratiometric images were generated and analyzed by using ImageJ (Fiji) software.

Statistical analyses

Data are expressed as mean \pm SD, if not stated otherwise. Statistical significance between groups was determined by unpaired Student's *t* test or two-way ANOVA followed by Tukey's multiple comparisons test. The levels of statistical significance considered were: * $p < 0.05$, ** $p < 0.01$, *** $p < 0.001$ and **** $p < 0.0001$. Statistical analyzes were performed using the Prism v.7.0 software (GraphPad, San Diego, CA).

Acknowledgements

We thank the patient and their family for their contribution to the study, Marc Thiry (University of Liege, Belgium) for his invaluable advice for TEM analysis. We thank the breeding facility from the University of Montpellier (RAM-CECEMA) for their help in animal breeding and handling. We thank the Electronic Microscopy facilities of the Institut des Neurosciences de Montpellier for TEM acquisition. P.P. is grateful to C. degli Scrovegni for her continuous support.

Disclosure statement

No potential conflict of interest was reported by the author(s).

Funding

The work was supported by the AFM-T  l  thon [Ignition]; Eye Hope Foundation; Fondation Pour l'Audition [RD-2019-13]; Fondation de France; FISM—Fondazione Italiana Sclerosi Multipla—cod.2022/R-Multi/050 and co-financed with the '5 per mille' public funding; A-ROSE (Associazione Ricerca Oncologica Sperimentale Estense); external resources of the University of Montpellier; Agence Nationale pour la Recherche [ANR-12-JSV1-0008-01]; The Snow Foundation; local funds from the University of Ferrara Italian Ministry of Education, University and Research [PRIN, 2017 E5L5P3]; Italian Association for Cancer Research [IG-23670]; Italian Association for Cancer Research [AIRC, 27938]; Italian Association for Cancer Research [AIRC, MFAG-29087]; Retina France.

Data availability statement

The data of this study is available from the corresponding authors upon reasonable request.

ORCID

Simone Patergnani  <http://orcid.org/0000-0001-7951-9267>
 Alberto Danese  <http://orcid.org/0000-0002-0833-9987>
 Ren   Val  ro  <http://orcid.org/0000-0002-2176-3280>
 Paolo Pinton  <http://orcid.org/0000-0001-7108-6508>
 Benjamin Delprat  <http://orcid.org/0000-0002-2457-6923>
 Elodie M. Richard  <http://orcid.org/0000-0002-4255-4699>

References

- [1] Fonseca SG, Fukuma M, Lipson KL, et al. WFS1 is a novel component of the unfolded protein response and maintains homeostasis of the endoplasmic reticulum in pancreatic beta-cells. *J Biol Chem.* 2005;280:39609–39615. doi: 10.1074/jbc.M507426200
- [2] Barrett TG, Bunday SE, Macleod AF. Neurodegeneration and diabetes: UK nationwide study of Wolfram (DIDMOAD) syndrome. *Lancet.* 1995;346(8988):1458–1463. doi: 10.1016/S0140-6736(95)92473-6
- [3] Rigoli L, Bramanti P, Di Bella C, et al. Genetic and clinical aspects of wolfram syndrome 1, a severe neurodegenerative disease. *Pediatr Res.* 2018;83(5):921–929. doi: 10.1038/pr.2018.17
- [4] de Heredia ML, Cl  ries R, Nunes V, et al. Genotypic classification of patients with Wolfram syndrome: insights into the natural history of the disease and correlation with phenotype. *Genet Med.* 2013;15(7):497–506. doi: 10.1038/gim.2012.180
- [5] de Muijnck C, Brink JBT, Bergen AA, et al. Delineating Wolfram-like syndrome: a systematic review and discussion of the WFS1-associated disease spectrum. *Surv Ophthalmol.* 2023;68(4):641–654. doi: 10.1016/j.survophthal.2023.01.012
- [6] Eiberg H, Hansen L, Kjer B, et al. Autosomal dominant optic atrophy associated with hearing impairment and impaired glucose regulation caused by a missense mutation in the WFS1 gene. *J Med Genet.* 2006;43(5):435–440. doi: 10.1136/jmg.2005.034892
- [7] Val  ro R, Bannwarth S, Roman S, et al. Autosomal dominant transmission of diabetes and congenital hearing impairment secondary to a missense mutation in the WFS1 gene. *Diabet Med.* 2008;25(6):657–661. doi: 10.1111/j.1464-5491.2008.02448.x
- [8] Richard EM, Brun E, Korchagina J, et al. Wfs1E864K knock-in mice illuminate the fundamental role of Wfs1 in endocochlear potential production. *Cell Death Dis.* 2023;14(6):387. doi: 10.1038/s41419-023-05912-y
- [9] Cagalinec M, Liiv M, Hodurova Z, et al. Role of mitochondrial dynamics in neuronal development: mechanism for Wolfram syndrome. *PLOS Biol.* 2016;14(7):e1002511. doi: 10.1371/journal.pbio.1002511
- [10] Angebault C, Fauconnier J, Patergnani S, et al. ER-mitochondria cross-talk is regulated by the Ca²⁺ sensor NCS1 and is impaired in Wolfram syndrome. *Sci Signal.* 2018;11(553):11. doi: 10.1126/scisignal.aaq1380
- [11] Crouzier L, Danese A, Yasui Y, et al. Activation of the sigma-1 receptor chaperone alleviates symptoms of Wolfram syndrome in preclinical models. *Sci Transl Med.* 2022;14(631):eabh3763. doi: 10.1126/scitranslmed.abh3763
- [12] Delprat B, Maurice T, Delettre C. Wolfram syndrome: MAMs' connection? *Cell Death Dis.* 2018;9(3):364. doi: 10.1038/s41419-018-0406-3
- [13] K  ks S, Overall RW, Ivask M, et al. Silencing of the WFS1 gene in HEK cells induces pathways related to neurodegeneration and mitochondrial damage. *Physiol Genomics.* 2013;45(5):182–190. doi: 10.1152/physiolgenomics.00122.2012
- [14] Zatyka M, Rosenstock TR, Sun C, et al. Depletion of WFS1 compromises mitochondrial function in hiPSC-derived neuronal

- models of Wolfram syndrome. *Stem Cell Rep.* 2023;18(5):1090–1106. doi: [10.1016/j.stemcr.2023.04.002](https://doi.org/10.1016/j.stemcr.2023.04.002)
- [15] Crouzier L, Richard EM, Diez C, et al. Morphological, behavioral and cellular analyses revealed different phenotypes in Wolfram syndrome *wfs1a* and *wfs1b* zebrafish mutant lines. *Hum Mol Genet.* 2022;31(16):2711–2727. doi: [10.1093/hmg/ddac065](https://doi.org/10.1093/hmg/ddac065)
- [16] Crouzier L, Richard EM, Diez C, et al. NCS1 overexpression restored mitochondrial activity and behavioral alterations in a zebrafish model of Wolfram syndrome. *Mol Ther Methods Clin Dev.* 2022;27:295–308. doi: [10.1016/j.omtm.2022.10.003](https://doi.org/10.1016/j.omtm.2022.10.003)
- [17] Zuleger N, Kelly DA, Richardson AC, et al. System analysis shows distinct mechanisms and common principles of nuclear envelope protein dynamics. *J Cell Bio.* 2011;193(1):109–123. doi: [10.1083/jcb.201009068](https://doi.org/10.1083/jcb.201009068)
- [18] Giorgi C, Bouhamida E, Danese A, et al. Relevance of autophagy and mitophagy dynamics and markers in neurodegenerative diseases. *Biomedicines.* 2021;9(2):149. doi: [10.3390/biomedicines9020149](https://doi.org/10.3390/biomedicines9020149)
- [19] Hernandez G, Thornton C, Stotland A, et al. MitoTimer. *Autophagy.* 2013;9(11):1852–1861. doi: [10.4161/auto.26501](https://doi.org/10.4161/auto.26501)
- [20] Patergnani S, Marchi S, Rimessi A, et al. Prkcb/protein kinase C, beta and the mitochondrial axis as key regulators of autophagy. *Autophagy.* 2013;9(9):1367–1385. doi: [10.4161/auto.25239](https://doi.org/10.4161/auto.25239)
- [21] Klionsky DJ, Abdel-Aziz AK, Abdelfatah S, et al. Guidelines for the use and interpretation of assays for monitoring autophagy (4th edition)1. *Autophagy.* 2021;17:1–382. doi: [10.1080/15548627.2020.1797280](https://doi.org/10.1080/15548627.2020.1797280)
- [22] Tranebjærg L, Barrett T, Rendtorff ND WFS1 Wolfram syndrome spectrum disorder. In: Adam MP, Everman DB, Mirzaa GM, Pagon RA, Wallace SE, Bean LJ, Gripp KW, Amemiya A, editor. *GeneReviews*®. Seattle (WA): University of Washington, Seattle;1993. cited 2022 Sep 1]. Available from: <http://www.ncbi.nlm.nih.gov/books/NBK4144/>
- [23] Giorgi C, Marchi S, Pinton P. The machineries, regulation and cellular functions of mitochondrial calcium. *Nat Rev Mol Cell Biol.* 2018;19(11):713–730. doi: [10.1038/s41580-018-0052-8](https://doi.org/10.1038/s41580-018-0052-8)
- [24] Giacomello M, Pellegrini L. The coming of age of the mitochondria-ER contact: a matter of thickness. *Cell Death Differ.* 2016;23(9):1417–1427. doi: [10.1038/cdd.2016.52](https://doi.org/10.1038/cdd.2016.52)
- [25] Rossi A, Pizzo P, Filadi R. Calcium, mitochondria and cell metabolism: a functional triangle in bioenergetics. *Biochim Biophys Acta, Mol Cell Res.* 2019;1866(7):1068–1078. doi: [10.1016/j.bbamcr.2018.10.016](https://doi.org/10.1016/j.bbamcr.2018.10.016)
- [26] Yang M, Li C, Yang S, et al. Mitochondria-associated ER membranes – the origin Site of autophagy. *Front Cell Dev Biol.* 2020;8:595. doi: [10.3389/fcell.2020.00595](https://doi.org/10.3389/fcell.2020.00595)
- [27] Liu J, Yang J. Mitochondria-associated membranes: a hub for neurodegenerative diseases. *Biomed Pharmacother.* 2022;149:112890. doi: [10.1016/j.biopha.2022.112890](https://doi.org/10.1016/j.biopha.2022.112890)
- [28] Cárdenas C, Miller RA, Smith I, et al. Essential regulation of cell bioenergetics by constitutive InsP3 receptor Ca²⁺ transfer to mitochondria. *Cell.* 2010;142(2):270–283. doi: [10.1016/j.cell.2010.06.007](https://doi.org/10.1016/j.cell.2010.06.007)
- [29] Missiroli S, Bonora M, Patergnani S, et al. PML at mitochondria-associated membranes is critical for the repression of autophagy and cancer development. *Cell Rep.* 2016;16(9):2415–2427. doi: [10.1016/j.celrep.2016.07.082](https://doi.org/10.1016/j.celrep.2016.07.082)
- [30] Ahumada-Castro U, Silva-Pavez E, Lovy A, et al. MTOR-independent autophagy induced by interrupted endoplasmic reticulum-mitochondrial Ca²⁺ communication: a dead end in cancer cells. *Autophagy.* 2018;15(2):358–361. doi: [10.1080/15548627.2018.1537769](https://doi.org/10.1080/15548627.2018.1537769)
- [31] Gelmetti V, De Rosa P, Torosantucci L, et al. PINK1 and BECN1 relocalize at mitochondria-associated membranes during mitophagy and promote ER-mitochondria tethering and autophagosome formation. *Autophagy.* 2017;13(4):654–669. doi: [10.1080/15548627.2016.1277309](https://doi.org/10.1080/15548627.2016.1277309)
- [32] Vollrath JT, Sechi A, Dreser A, et al. Loss of function of the ALS protein SigR1 leads to ER pathology associated with defective autophagy and lipid raft disturbances. *Cell Death Dis.* 2014;5(6):e1290. doi: [10.1038/cddis.2014.243](https://doi.org/10.1038/cddis.2014.243)
- [33] Aman Y, Schmauck-Medina T, Hansen M, et al. Autophagy in healthy aging and disease. *Nat Aging.* 2021;1(8):634–650. doi: [10.1038/s43587-021-00098-4](https://doi.org/10.1038/s43587-021-00098-4)
- [34] Fernandes T, Resende R, Silva DF, et al. Structural and functional alterations in mitochondria-associated membranes (MAMs) and in mitochondria activate stress response mechanisms in an in vitro model of alzheimer's disease. *Biomedicines.* 2021;9(8):881. doi: [10.3390/biomedicines9080881](https://doi.org/10.3390/biomedicines9080881)
- [35] Johri A, Connection Lost CA. Connection Lost, MAM: errors in ER-mitochondria connections in neurodegenerative diseases. *Brain Sci.* 2021;11(11):1437. doi: [10.3390/brainsci11111437](https://doi.org/10.3390/brainsci11111437)
- [36] Degechisa ST, Dabi YT, Gizaw ST. The mitochondrial associated endoplasmic reticulum membranes: A platform for the pathogenesis of inflammation-mediated metabolic diseases. *Immunity Inflamm & Disease.* 2022;10(7):e647. doi: [10.1002/iid3.647](https://doi.org/10.1002/iid3.647)
- [37] Li L, Venkataraman L, Chen S, et al. Function of WFS1 and WFS2 in the central nervous System: implications for Wolfram Syndrome and alzheimer's disease. *Neurosci Biobehav Rev.* 2020;118:775–783. doi: [10.1016/j.neubiorev.2020.09.011](https://doi.org/10.1016/j.neubiorev.2020.09.011)
- [38] Delettre C, Lenaers G, Griffoin J-M, et al. Nuclear gene OPA1, encoding a mitochondrial dynamin-related protein, is mutated in dominant optic atrophy. *Nat Genet.* 2000;26(2):207–210. doi: [10.1038/79936](https://doi.org/10.1038/79936)
- [39] Del Dotto V, Carelli V. Dominant Optic Atrophy (DOA): modeling the kaleidoscopic roles of OPA1 in mitochondrial homeostasis. *Front Neurol.* 2021;12:681326. doi: [10.3389/fneur.2021.681326](https://doi.org/10.3389/fneur.2021.681326)
- [40] Zaman M, Shutt TE. The role of impaired mitochondrial dynamics in MFN2-mediated pathology. *Front Cell Dev Biol.* 2022 [cited 2023 Sep 1];10. Available from: <https://doi.org/10.3389/fcell.2022.858286>
- [41] Su T-P, Hayashi T, Maurice T, et al. The sigma-1 receptor chaperone as an inter-organelle signaling modulator. *Trends Pharmacol Sci.* 2010;31(12):557–566. doi: [10.1016/j.tips.2010.08.007](https://doi.org/10.1016/j.tips.2010.08.007)
- [42] Angebault C, Gueguen N, Desquret-Dumas V, et al. Idebenone increases mitochondrial complex I activity in fibroblasts from LHON patients while producing contradictory effects on respiration. *BMC Res Notes.* 2011;4(1):557. doi: [10.1186/1756-0500-4-557](https://doi.org/10.1186/1756-0500-4-557)
- [43] Morciano G, Patergnani S, Pedriali G, et al. Impairment of mitophagy and autophagy accompanies calcific aortic valve stenosis favouring cell death and the severity of disease. *Cardiovasc Res.* 2022;118(11):2548–2559. doi: [10.1093/cvr/cvab267](https://doi.org/10.1093/cvr/cvab267)
- [44] Kilkenny C, Browne WJ, Cuthill IC, et al. Improving bioscience research reporting: the ARRIVE guidelines for reporting animal research. *J Pharmacol Pharmacother.* 2010;1(2):94–99. doi: [10.4103/0976-500X.72351](https://doi.org/10.4103/0976-500X.72351)
- [45] Bonora M, Giorgi C, Bononi A, et al. Subcellular calcium measurements in mammalian cells using jellyfish photoprotein aequorin-based probes. *Nat Protoc.* 2013;8(11):2105–2118. doi: [10.1038/nprot.2013.127](https://doi.org/10.1038/nprot.2013.127)
- [46] Koopman WJH, Visch H-J, Smeitink JAM, et al. Simultaneous quantitative measurement and automated analysis of mitochondrial morphology, mass, potential, and motility in living human skin fibroblasts. *Cytometry Part A.* 2006;69A(1):1–12. doi: [10.1002/cyto.a.20198](https://doi.org/10.1002/cyto.a.20198)
- [47] Sage D, Donati L, Soulez F, et al. DeconvolutionLab2: an open-source software for deconvolution microscopy. *Methods.* 2017;115:28–41. doi: [10.1016/j.ymeth.2016.12.015](https://doi.org/10.1016/j.ymeth.2016.12.015)
- [48] Kirshner H, Aguet F, Sage D, et al. 3-D PSF fitting for fluorescence microscopy: implementation and localization application. *J Microsc.* 2013;249(1):13–25. doi: [10.1111/j.1365-2818.2012.03675.x](https://doi.org/10.1111/j.1365-2818.2012.03675.x)
- [49] Bolte S, Cordelières FP. A guided tour into subcellular colocalization analysis in light microscopy. *J Microsc.* 2006;224(3):213–232. doi: [10.1111/j.1365-2818.2006.01706.x](https://doi.org/10.1111/j.1365-2818.2006.01706.x)
- [50] Patergnani S, Bonora M, Ingusci S, et al. Antipsychotic drugs counteract autophagy and mitophagy in multiple sclerosis. *Proc Natl Acad Sci USA.* 2021;118(24):e2020078118. doi: [10.1073/pnas.2020078118](https://doi.org/10.1073/pnas.2020078118)